Elucidation of the Solid Electrolyte Interphase Formation Mechanism in Micro-Mesoporous Hard-Carbon Anodes

Hande Alptekin[1], Heather Au[1], Emilia Olsson[1,2,3], Jonathon Cottom[4], Anders CS Jensen[1,2], Thomas F. Headen[5], Alan J Drew[2], Qiong Cai[3], Maria-Magdalena Titirici[1*], Maria Crespo Ribadeneyra[1*]

[1]*Department of Chemical Engineering, Imperial College London, London SW7 2AZ, UK.*
[2]*School of Physics and Astronomy and Materials Science and Materials Research Institute, Queen Mary University of London, London E1 4NS, UK.*
[3]*Department of Chemical and Process Engineering, University of Surrey, Guildford, GU2 7XH, UK.*
[4]*Department of Physics & Astronomy, University College London, Gower Street, London WC1E 6BT, UK.*
[5]*ISIS Pulsed Neutron and Muon Source, Rutherford Appleton Laboratory, STFC, Didcot OX11 0QX, UK.*
* *Corresponding authors. Email: mcrespo1@ic.ac.uk ; m.titirici@imperial.ac.uk*

ABSTRACT

The microstructure of hard carbons can be designed to maximise their performance as anodes for sodium-ion batteries. However, the nature of the electrolyte is also decisive in the capacity and long-term stability that these materials can achieve. Here, hard carbons with tailored bimodal porosities, presenting an extended pore network of internal micropores interconnected through mesopores, are studied as sodium-ion battery anodes and the evolution of their solid electrolyte interphase (SEI) is analysed in three different electrolytes ($NaPF_6$ in an ether-based solvent, and $NaPF_6$ or $NaClO_4$ in a carbonate-based system). Combining experimental results with density functional theory calculations, we propose that formation of the solid electrolyte interphase is mainly controlled by the decomposition of the salt anion. This process occurs through the intermediate functionalisation of the carbon surface by the decomposed anion fragments. We suggest that it is the innermost SEI sub-layer that governs the performance and long-term stability of the anode. While the presence of a fluorine-containing salt appears to have a determining role in the SEI stability, the electrochemical decomposition of carbonate-based solvents can generate unwanted interfacial resistance that is eventually detrimental for the long-term stability. In contrast, the cyclability of the ether-based system is enhanced and the interphase is maintained almost intact once the first fluorine-rich SEI layer is formed.

INTRODUCTION

Lithium-ion batteries were commercialised in the early 1990's;[1] however, the cost of raw materials has almost doubled since then, and it is expected to continue increasing with demand and further ore deployment.[2] It is therefore imperative to advance the development and understanding of alternative battery chemistries, both to offset the consumption of critical materials and the global reliance on only one type of technology. Sodium-ion batteries (NIBs) are a promising alternative for large-scale energy storage due to the natural abundance, widespread distribution, low cost, and excellent materials sustainability in comparison to lithium-reliant technologies.[3]

Unlike lithium, sodium can only intercalate minimally into graphite. For NIBs, hard carbon (HC) is the preferred anode candidate, since its disordered and non-graphitizable turbostratic structure can provide many sites for sodium storage. Sodium adsorption and storage occur at the randomly-oriented and expanded graphene layers, edge and basal defects, and at the micropores within the graphitic fragments formed by the graphene stacks.[4] Great effort has been devoted to understand and attribute a voltage range to sodium storage within each of these microstructural features. Although still under some degree of debate, in general, the capacity of HC evolves through two distinct regimes: a high-voltage sloping region, attributed mostly to defects and intercalation between expanded layers, and a low-voltage plateau (< 0.1V $vs.$ Na$^+$/Na) revealing sodium storage inside the native pores (micropores or nanopores) of the HC structure. Many of the processes observed within the sloping region have been regarded as irreversible or related to the formation of the solid electrolyte interphase (SEI) on the accessible surface area of the carbons during the first discharge cycle (sodium insertion).[5][6]

Most synthesis strategies aim for carbons with a limited surface area but with an enhanced concentration of internal micropores, accessible solely to sodium ions, to boost the initial Coulombic efficiency and the reversible specific capacity (generally $\sim$300 mA h g^{-1}).[7,8] Both the carbon precursor pre-treatment and the consecutive annealing temperature play a crucial role in the microstructure. The pre-treatment of biomass derivatives at $\sim$200 °C seems to enable larger micropores (and thus better interconnected) than those achieved through the direct thermal activation of the same feedstock.[9] Au et $al.$[10] reported a sharp decrease in surface area with increasing annealing temperature (1000-1900 °C), and the formation of larger internal pores as a consequence of the growth of the lateral dimensions of the graphitic fragments surrounding the pores. Nevertheless, above a certain temperature ($\sim$1500 °C), further graphitisation becomes detrimental due to the reduction of the interlayer spacing and the consequent narrowing of the paths for sodium to access the pores.

In this context, maximising the interconnectivity of closed pores for Na-ion storage by maintaining enlarged interlayer distances, number of defects and accessible diffusion pathways enables precise tuning of the reversible capacity of HCs. In turn, this strategy produces NIBs with larger energy densities and extended service life.[11] However, tuning the texture of carbons does not suffice to maximise the performance of batteries, both in terms of the initial delivered capacity and long-term stability. Factors such as the nature of electrolyte determine the composition of the SEI, as this is formed upon the decomposition of the salt and solvent.

Excellent studies have been published regarding the role of fluorine-containing solvents or additives in the stability of the SEI for HCs [12][13] and TiO$_2$ anodes,[14] the stabilising role of glymes for several types of electrodes,[15][16] the formation of ethylene dicarbonate, NaF and Na$_2$CO$_3$ as primary constituents of the SEI when carbonate-based electrolytes are employed, and the similarity of such mosaic-type SEI with that observed in lithium-ion batteries.[17] Nevertheless, fewer studies are found reporting the role of the salt and solvents on both the

formation mechanism and properties of the SEI, [18] [19] [20][21] and there are even less examples were experiments and simulations are combined together to understand how exactly the SEI starts developing and what triggers stability or constant degradation.

Here, we report solvothermally prepared HCs with tailored bimodal porosities (micro- and mesopores) for Na-ion batteries. Through the secondary mesoporous network derived from a soft template introduced during the hydrothermal treatment, we aim to enhance and widen the connectivity between the internal micropore network (Figure 1a). This strategy is expected to facilitate Na^+ diffusion over a larger length scale and to reach higher capacities than those observed for standard hard carbons annealed at equivalent temperatures. To understand and improve the performance of these materials, the formation of the SEI in three electrolyte systems (varying both salt and solvent) is studied and related to their electrochemical capacity and long-term Na-storage retention. The intrinsic properties of the salts and solvents (e.g. donor and acceptor numbers and redox potentials) are analysed and the pathway of the SEI formation is proposed. Corroborated by computational studies, our findings suggest that SEI formation is mainly determined by decomposition of the salt anion and that it occurs through the intermediate functionalisation of the carbon surface. The total amount of Na irreversibly consumed, and also the formation of a conductive and protective SEI layer, can be thus tailored through the choice of electrolyte mixture. In all the electrolyte systems the SEI layer presents a layered structure, consisting of an inorganic innermost layer covered by an organic-derived shell. We suggest that it is the inorganic internal SEI sub-layer that governs the performance and long-term stability of the anode. While the presence of a fluorine-containing salt appears to have a determining role in the SEI stability, the electrochemical decomposition of carbonate-based solvents can generate unwanted interfacial resistance that is eventually detrimental for the long-term stability. In contrast, in an ether-based solvent, the cyclability of the cell is enhanced and the interphase remains almost intact once the first fluorine-rich SEI layer is formed.

RESULTS
Soft templated hard carbons: templated closed porosity and structural evolution with temperature
To obtain hard carbons with tailored porosities, phloroglucinol and glyoxal were dissolved in ethanol and solvothermally carbonised in the presence of a soft templating agent (Pluronic F127). Due to the equilibrium between carboxylic acid and geminal-diol groups, glyoxylic acid can both catalyse the polymerisation and generate crosslinks between the phenol groups of phloroglucinol[22][23] (Figure 1a). In the presence of Pluronic F127 micelles (Figure 1a), the crosslinked resin develops around the templated domains (20-40 nm), and micro-mesoporous structures are expected once the sacrificial polymer is removed by high-temperature pyrolysis. The resulting carbon (ST200) was therefore pyrolyzed at 1000 °C, 1300 °C and 1500 °C, and labelled accordingly as ST1000, ST1300 and ST1500. The spherical particles, with diameters ranging from 2 to 4 μm (Figure S1), remained unaltered after carbonisation for all temperatures (Figure 1).
Internal or 'closed pores', inaccessible to gas molecules but accessible to Na^+ ions, are responsible for sodium storage in HCs at low potentials,[24,25] and their diameter can be derived from the region at 0.2 Å^{-1} in the total small angle neutron scattering (SANS) patterns (Figure 1b) using the Guinier-Porod model[26,27] (equation 1 in ESI). Micropores between 1.8 and 2.3 nm and mesopores around 25-40 nm were observed for all materials (Figure 1c).
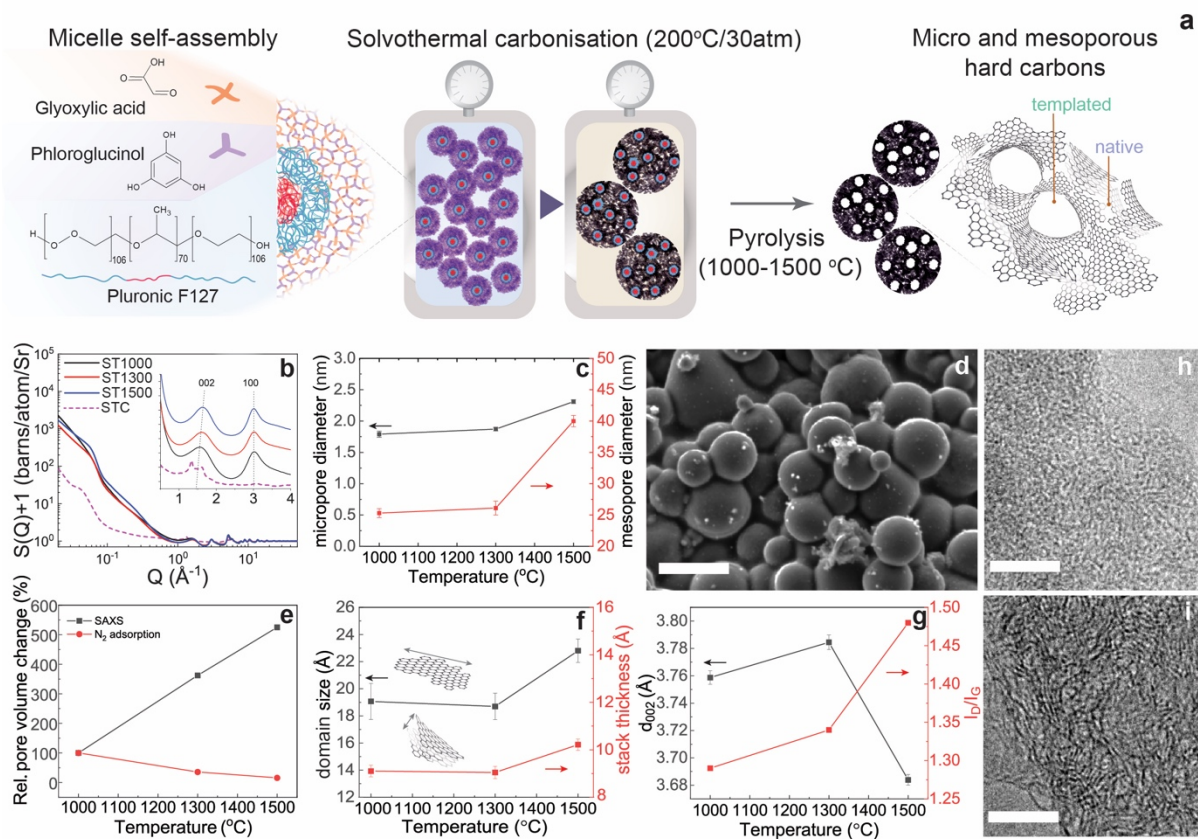
Figure 1. (a) *Schematic of the bimodal porous structure of the soft templated carbons.* **(b)** *Small angle neutron structure factor (Q) of the carbon precursor after solvothermal carbonisation (STC) and after subsequent high temperature pyrolysis at 1000, 1300 and 1500 °C (ST1000, ST1300 and ST1500, respectively). Inset shows the 002 and 100 peaks related to the local graphitic domains.* **(c)** *Pore diameters derived from SAXS corresponding to the native HC micropores and templated mesopores;* **(d)** *Representative SEM of ST particles after 1000°C annealing. Scale bar is 5 μm;* **(e)** *Relative change in the pore volume probed by N_2 gas adsorption and the intensity of the Guinier plateau in the small angle region weighted by pore volume;* **(f)** *Basal domain size, stack thickness and* **(g)** *average spacing between the graphitic basal planes (002) determined from the width of the 002 and 100 peaks of the total SAXS/WAXS patterns. Additional SAXS/WAXS data and example model fits are shown in Fig. SX (ESI); I_D/I_G ratio derived from Raman spectroscopy. TEM images of* **(h)** *ST1000 and* **(i)** *ST1500 showing the evolution of graphitic domains. Scale bars are 20 nm.*

The mesopores, ascribed to the templating strategy, increase in diameter with increasing temperature, most significantly above 1300°C (60%). The diameter of the micropores changes from 1.9 to 2.3 nm (40%), suggesting that micropore growth is more limited or that these combine to form significantly larger pores during the annealing process. By comparing the relative total pore volume derived from small angle X-ray scattering SAXS (Figure 1e), a five-fold increment is observed between 1000 °C and 1500°C (Figure 1e). Notably, a substantial volume change within this temperature range is not observed for other HCs produced without a templating agent.[5] The micropore dimensions proved similar to the lateral size of the graphitic fragments (Figure 1f) derived from SAXS (Figure S2). In agreement with our previous work,[10] increasing the pyrolysis temperature within this range promotes the evolution of a greater number of slightly longer and thicker graphitic stacks (Figure 1f) that form the walls of Na-storing closed micropores. Higher pyrolysis temperatures are thus associated with an increase in Na-ion pore storage capacity, provided that enlarged interlayer distances and pore access pathways are still available.

Although the evolution towards a more ordered structure is promoted with increasing temperature, between 1000 and 1300°C there seems to be little change in the size and thickness

4

of the graphitic fragments. Additionally, the interlayer distance (Figure 1g, d_{002}) corresponding to the (002) diffraction of the graphitic layers at 1.8 Å^{-1} (inset Figure 1b) remains enlarged even at 1300°C (3.78 Å) and only drops to 3.68 Å at 1500°C. Such behaviour can be attributed to both the presence of a templating agent and the pre-crosslinking of the glyoxal-phloroglucinol resin; a 'pillar effect' has been observed with HCs produced from crosslinked precursors,[9][28] preventing the shrinkage and stacking of the graphene-like layers, resulting in less dense graphitic domains with enlarged interlayer distances and larger pores once carbonised.

To further investigate porosity, gas-accessible pores (equal to or larger than 0.4 nm[29]) were analysed through N_2 adsorption-desorption isotherms (Figure S3 in ESI). As expected, the specific surface area (mostly constituted by mesopores, see Figure S3b in ESI) displayed a decreasing trend with the annealing temperature (181, 66 and 21 m^2/g for ST100, ST1300 and ST1500, respectively). This trend opposes that observed by small-angle scattering data, suggesting that the majority of pores are closed off during pyrolysis.[8] It is worth noting that despite their considerable size (25-40 nm), the mesopores observed through neutron scattering seem to also be mostly closed, as those that are observed through N_2-adsorption present a pore size distribution centred around 10-15nm (Figure S3a) Nevertheless, these surface area values remain higher than those observed for non-templated HCs annealed at equivalent temperatures, which become virtually non-porous above 1300 °C.[10][30][31] Such behaviour indicates that the synthesis methodology is indeed preventing the compaction of the structure with increasing temperature.

The development of structural ordering with temperature was corroborated by TEM (Figure 1h and 1i). Interestingly, the presence of the templated micropores is not observable through TEM, as it would be expected for templated pores aligned one to another and having identical shapes.[32] Some disordered domains and short graphene fringes, typical of hard carbons, are observed at 1000 °C (Figure 1h). Above 1300 °C, more graphitic stacks with random orientation start to be observed (Figure S4). At 1500 °C (Figure 1i), the graphitic fringes become overall more evident and aligned, suggesting the development of a higher number of more ordered and larger graphitic domains. These results are consistent with the increasing in-plane ordering implied by the Raman I_D/I_G ratio increment (Figure 1g),[33] indicating the reduction of defects (see Figure S5 for details) and the removal of polar surface groups with temperature (Figure S6 in ESI).

Electrochemical performance in Na-ion half cells
The impact of the structural characteristics of the soft templated carbons on their electrochemical performance was evaluated in half cells using sodium metal as the counter electrode and 1M NaPF$_6$ in EC:DMC as the electrolyte, between 0.005 and 3V. The galvanostatic discharge-charge profiles at 30 mA g^{-1} (Figure 2a) show a common behaviour: discharge curves (sodium insertion) display a sloping region above 0.1V, predominantly associated with adsorption at edge or basal defects or insertion into enlarged interlayer spaces, and a flatter plateau region below 0.1V, arising from Na storage within internal or 'closed' pores (Figure 2d-f). Overall, ST1500 presents the highest initial Coulombic efficiency (65%, Figure 2h) and first and second cycle capacities (523 and 354 mAh g^{-1}, respectively), predominantly plateau-derived, consistent with having the highest internal pore volume and the lowest surface area and number of defects. In contrast, ST1000 shows a large and mostly sloped capacity in the first cycle, which decreases substantially in the second cycle. This large and irreversible consumption of Na is consistent with the high surface area of ST1000 that is accessible for the decomposition of the electrolyte and subsequent formation of the SEI; the same phenomenon is observed, to a lesser extent, in both ST1300 and ST1500, as they have a lower presence of open porosity.
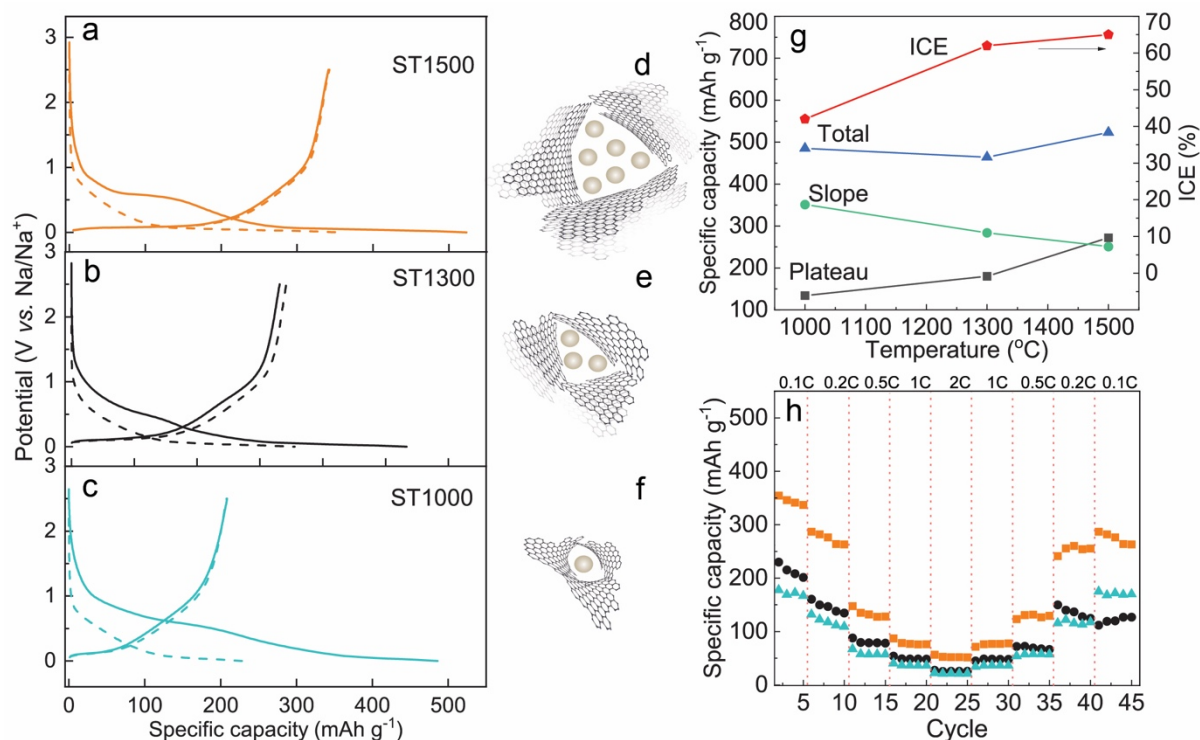
Figure 2. Galvanostatic discharge-charge profiles at 30 mAg^{-1} showing the first (solid lines) and second (dashed lines) cycles for **(a)** ST5000 **(b)** ST1300 and **(c)** ST1000. Schematic of the closed porosity evolution with temperature: **(d)** ST1500, **(e)**ST1300 and **(f)**ST1000. **(g)** First cycle total, slope and plateau capacities, and initial Coulombic efficiency (ICE) for ST1000, ST1300 and ST1500; **(h)** Rate performance of the discharge capacities at 30, 60, 150, 300 and 600 mA g^{-1} for ST1500 (orange), ST1300 (black) and ST1000 (light blue); the dotted lines delimit each of these current densities.

A high-voltage plateau-like region appears at around 0.4-0.6V, even for the material annealed at 1500 °C (Figure 2a) owing to the decomposition of ester-based solvents into double alkyl carbonates.[34] This irreversible process is also observed in the first cycle of the cyclic voltammograms (CVs Figure S7). During the first discharge step, Na is consumed irreversibly, as manifested by the broad peaks appearing at 0.3-0.8V. In the subsequent cycles, the reduction and oxidation currents, observed closer to the lowest voltage limit and attributed to the reversible insertion and extraction of Na ions, become larger and steady only for ST1500. For ST1000 and ST1300, the Na trapping appears lessened, yet the storage of Na remains inefficient.

The specific capacity of the ST1500 carbon at the highest current density drops to a lesser extent than for the rest of carbons (Figure 2i, 57 mAh g^{-1} at 600 mA g^{-1} or 2C). At high current density most HCs display a near-zero capacity due to the excessive polarization of the electrodes and the restricted Na$^+$ diffusion occurring at high charging rates. The capacity retention at high current densities could be related to the connectivity between the meso- and micropores, with the larger templated pores facilitating fast diffusion of Na$^+$ into the smaller pores native to the disordered HC structure.

Solid electrolyte interphase (SEI) composition and long-term performance

With the aim of further stabilising the SEI through electrolyte engineering, and thus increasing the reversible capacity of the best performing material (ST1500), two additional electrolyte systems were screened. NaPF$_6$ was replaced by NaClO$_4$ for one of the systems, keeping the same solvent (EC:DMC), and for the second, EC:DMC was replaced with bis(2-methoxyethyl) ether (diglyme). The main differences between the salts are the ion mobility (NaClO$_4$ > NaPF$_6$),

the dissociation constant (NaClO$_4$ < NaPF$_6$) and the donor number (DN, DN$_{PF6-}$= 2.50) < DN$_{ClO4-}$= 8.4), all of which determine the ionic conductivity (in EC:DMC, σ_{NaClO4}= 5 Scm^{-1} σ_{NaPF6}= 6.5 Scm^{-1}).[35] A higher anion DN favours ion pair interactions, which leads to lower ionic conductivities and inhibits solvation.

With regard to the choice of solvents, diglyme is an ether-based solvent (C-O-C) while in the EC:DMC mixture, both molecules are carbonates with ester bonds (-O-C(=O)-O-), where EC is cyclic and DMC is linear. According to the electron acceptor-donor power of a solvent, a higher acceptor number (AN) implies better charge-accepting ability, while a higher DN reflects better solvation of the cation. Diglyme has a relatively low AN (~9.9) compared to the carbonates (~18),[36] yet its higher DN (19.2[37] *vs.* 16.4 or 17.2 for EC and DMC, respectively) has been associated with a compact and protective solvation shell that impedes contact ion pair interactions. Glymes have thus been identified as solvents that promote a stable SEI, both in positive and negative electrodes, and that are able to stabilise high specific surface area carbons. Nevertheless, the fundamental mechanism and cause of this improvement remains unclear and experimental data has not been fully contrasted with theoretical simulations.

When cycled at 30 mA g^{-1} (Figure 3, and fully summarised in Table S2), the NaClO$_4$/EC:DMC system presents the highest first cycle capacity but the worst long-term cyclability. The first cycle capacity of the NaPF$_6$ salt is higher in EC:DMC compared to diglyme, although changing to diglyme improves the initial Coulombic efficiency and gives excellent capacity retention (~70%) after 200 cycles (Figure 3a), suggesting the formation of a more stable SEI layer.[16] This lower initial capacity in diglyme compared with EC:DMC may arise from a certain degree of solvent co-intercalation within the expanded graphitic layers, limiting the overall amount of Na that the HC can accommodate. Co-intercalation of Na ions with different solvents has been widely observed in graphite,[38][39][40][41] but might be expected to a lesser extent in hard carbons because the highly crosslinked graphitic domains cannot accommodate the strain induced by the larger volume expansion. It is worth mentioning that the system employing NaClO$_4$ in diglyme was not tested due to the relentless impossibility of running the test. Such behaviour can be attributed to the inability of the diglyme, with a very low AN, of solvating the high DN ClO$_4^-$ anion, and thus, being unable to modulate its decomposition upon polarisation.[42]

Impedance spectra were recorded before and after the first charge/discharge cycle. From the Nyquist plots in Figure 3e-f, a higher overall resistance for both the NaPF$_6$ and NaClO$_4$/EC:DMC systems (higher x-intercept of the semicircle) is seen. In contrast, for the diglyme-based electrolyte (Figure 3d), a flattened semi-circle (low variation of impedance with frequency) is observed, that becomes even flatter upon three galvanostatic discharge/charge cycles (Figure S8 in ESI). This limited evolution of impedance in the NaPF$_6$/diglyme system corroborates the formation of a stable and conductive SEI during the first charge/discharge cycle, which remains mostly unaffected in consecutive cycles. In contrast, the impedance of the NaClO$_4$/EC:DMC system increases upon cycling, suggesting that the evolving SEI becomes more resistive. Eventually, only a low capacity of 100 mAh g^{-1} (44%) is retained after 200 cycles at 30 mA g^{-1}, indicating a decline in the charge transfer process at this constantly evolving interphase (Figure3c).
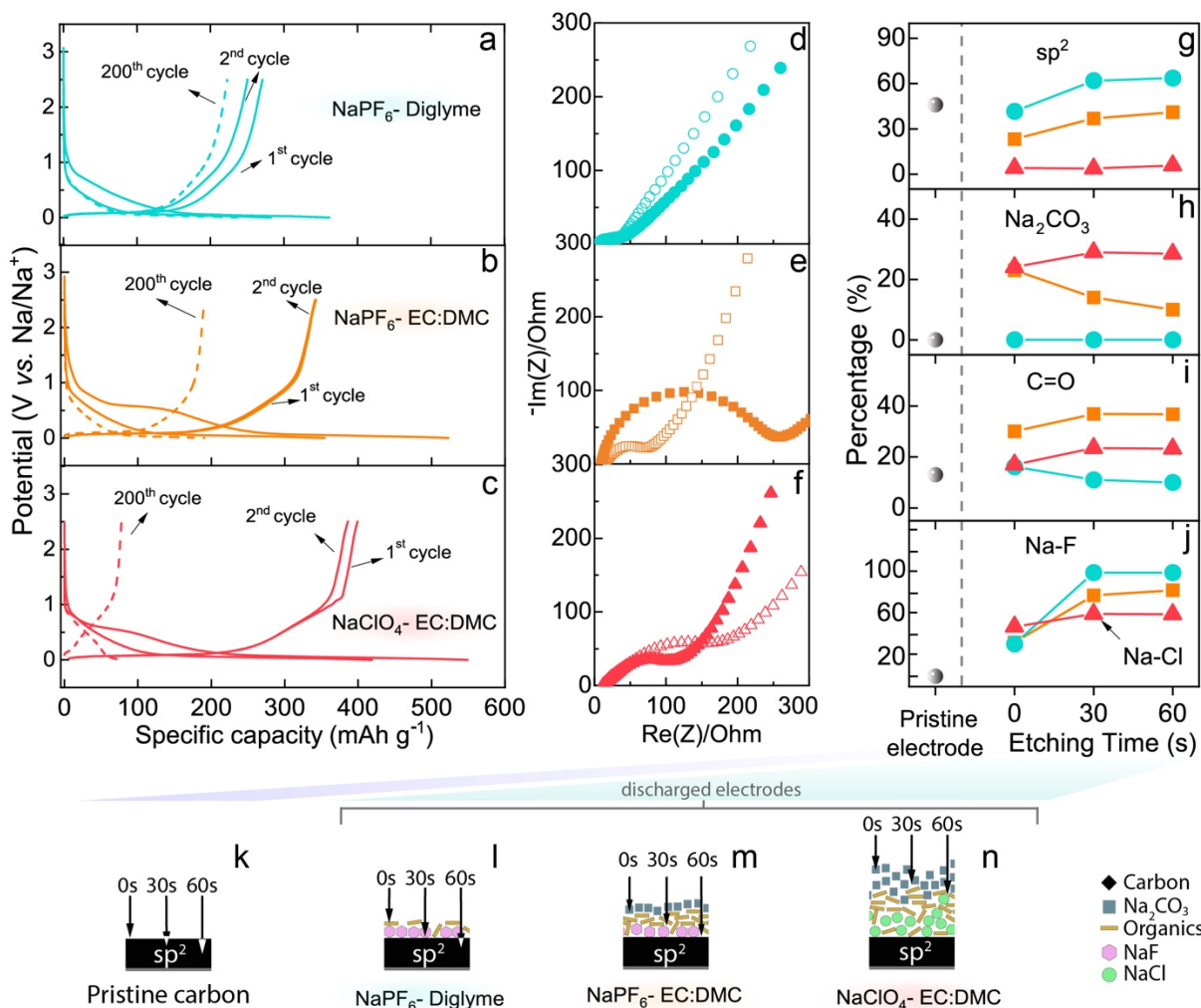
Figure 3. Galvanostatic discharge-charge profiles of ST1500 at 30 mAg^{-1} showing the capacity for the first, second (solid lines) and 200th cycle (dashed lines) in **(a)** 1M NaPF$_6$/Diglyme **(b)** 1M NaPF$_6$/EC:DMC and **(c)** 1M NaClO$_4$/EC:DMC; Corresponding electrochemical impedance spectroscopy (EIS) before (solid symbols) and after (open symbols) three discharge-charge cycles at 0.1mV s^{-1} in **(d)** 1M NaPF$_6$/Diglyme **(e)** 1M NaPF$_6$/EC:DMC and **(f)** 1M NaClO$_4$/EC:DMC. SEI depth composition analysis performed by recording XPS surveys after 30 and 60s of Ar$^+$ etching for electrodes before (light blue symbols) and after one galvanostatic discharge-charge cycle in 1M NaPF$_6$/Diglyme (pink), 1M NaPF$_6$/EC:DMC and (orange) and 1M NaClO$_4$/EC:DMC (green). The contribution (%) of the different environments were extracted from the high-resolution C1s core-level spectrum, to enable the comparison of the sp^2 C **(g)**, Na$_2$CO$_3$ **(h)** and C=O **(i)** bonds, while the NaF and NaCl **(j)** contributions were extracted from the F1s and Cl2p high-resolution spectra. Extracted from the XPS analysis, a scheme of the layered nature of each of the formed SEIs when the electrodes are discharged in the different electrolyte systems:**(k)** pristine carbon electrode before discharge, **(l)** in 1M NaPF$_6$/Diglyme, **(m)** in 1M NaPF$_6$/EC:DMC and **(n)** in 1M NaClO$_4$/EC:DMC.

The differences at the SEI level were substantiated by analysing the composition across the electrode/electrolyte interface with XPS (see full details of XPS characterisation in ESI). The cycled electrodes were progressively Ar$^+$ etched and a compositional depth profile was obtained by determining the percentage change of the sp^2 C (285.1 eV), Na$_2$CO$_3$ (290.2 eV) and C=O (289.2 eV) bond environments within the high-resolution C1s core-level spectrum, and the NaF (684 eV) and NaCl (200.5 eV) bonds in the F1s and Cl2p spectra, respectively (Figure 3 g-j). The sp^2 carbon environment of the C1s band is predominantly attributed to the pristine hard carbon which is buried underneath the SEI after cycling. With etching time, the percentage of the sp^2 contribution increases for both electrodes cycled in NaPF$_6$, while it remains close to zero for the NaClO$_4$ system.

8

In the case of the Na_2CO_3 environment, its presence can be attributed to the oxidative decomposition of the electrolyte and the C=O to the formation of polyesters derived from the solvent.[16,43] For the diglyme system, both bands remain extremely weak for all etching times, indicating a thin and homogeneous SEI layer with a very low amount of organic electrolyte decomposition products. In the case of the systems cycled in EC:DMC, for the one incorporating $NaPF_6$, the Na_2CO_3 percentage decreases sharply after only 30s, suggesting that Na_2CO_3 is predominantly distributed on the outermost layer of the SEI. In the case of the C=O band, the percentage increase with etching time suggests that polyester species are found mostly at the inner layer.

For the system incorporating $NaClO_4$, the resulting Na_2CO_3 layer appears to be thick enough not to change in composition with etching time and could be related to oxygen loss intrinsic to $NaClO_4$ decomposition. Although our findings through XPS etching are in line with the electrochemical performance, it is worth mentioning that through this technique, there is a large likelihood of introducing oxygen-containing functionalities during the etching step. Due to this limitation, further analysis is currently under development through ^{23}Na-Nuclear Magnetic Resonance (NMR) and Time-of-Flight Secondary Ion Mass Spectrometry (ToF-SIMS) for our follow up work.

Understanding the formation of the SEI

Density functional theory (DFT) calculations indicate that neither the adsorption of ClO_4^- ($E_{ads}=1.43$ eV) or PF_6^- ($E_{ads}=1.68$ eV) are energetically favoured on the basal plane of the carbon, but adsorption of anion fragments is possible (see table S4 in ESI for details of adsorption energies of all the possible fragments). Simulations of the anion fragmentation show that ClO_4^- dissociates through stepwise oxygen loss (Figure 4a) whilst in PF_6^-, fluorine fragments are successively detached (Figure 4b). In agreement with previous work,[44] as ClO_4^- fragments, oxygen groups can be easily incorporated into the carbon basal plane (Figure 4a.ii and iv); for the $NaClO_4$ system, the steady amount of Na_2CO_3 and C=O groups across the SEI depth determined by XPS is consistent with this assertion. Furthermore, the greater thickness of the ClO_4^--derived SEI could be attributed to the large oxygen loss that this anion undergoes as it decomposes. These oxygen moieties have been shown to subsequently promote energetically favourable Na adsorption[45] and the higher initial capacity observed in the $NaClO_4$/EC:DMC system compared with $NaPF_6$ could therefore potentially arise from these oxygen functionalities that are introduced through anion decomposition.
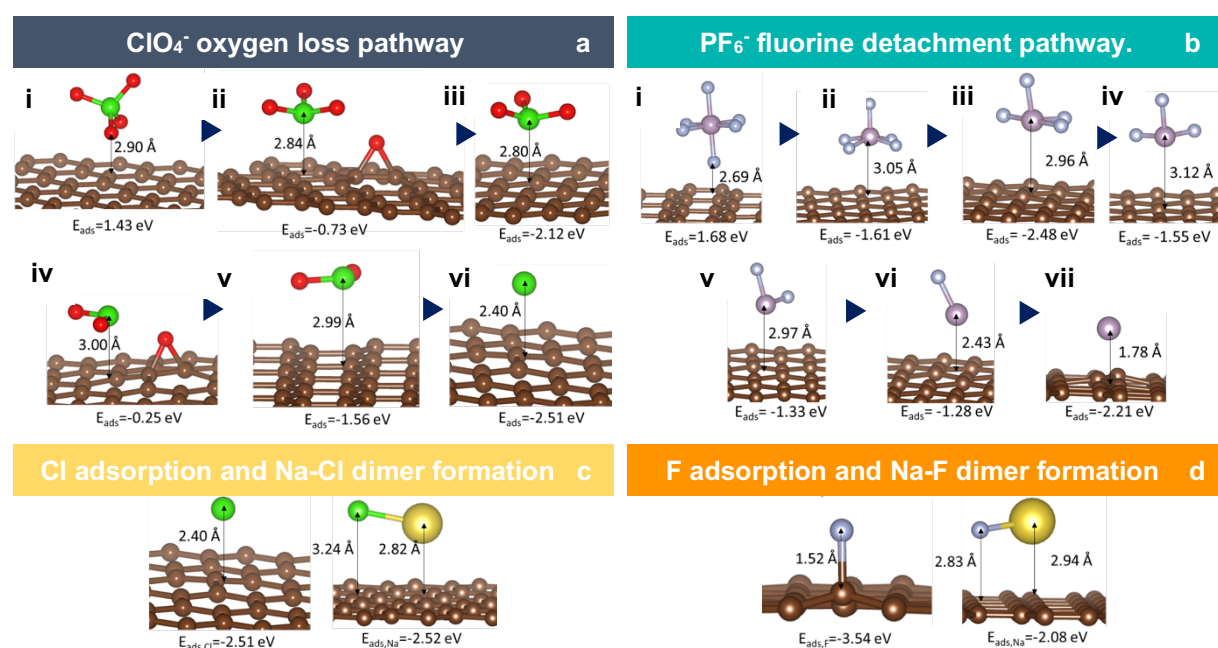
Figure 4. Optimised structures of a) ClO₄⁻ decomposition products on carbon, b) PF₆⁻ decomposition products on carbon, c) Cl adsorption and Na-Cl dimer formation, and d) F adsorption on carbon surface highlighting the puckering of the carbon lattice, and subsequent Na-F dimer formation. Brown spheres are carbon, green chlorine, yellow sodium, and grey fluorine.

The Cl and F fragments (Figures 4c and d) are both attracted to the carbon basal surface ($E_{ads,F}$=-3.54 eV, $E_{ads,Cl}$=-2.51 eV); in the case of F, the fragment seemingly binds to the carbon. When the carbon is fluorinated, it is observed that the F-C bond puckers the basal plane (Figures 4d.i). The favourable C-F bond formation is key to the passivating effect that fluorinated additives and salts have on carbonaceous anodes. For the Cl containing system, the Cl-C distance remains large (2.40 Å vs. 1.52 Å for F-C), in agreement with previous studies.[46]

The adsorption of Na in the vicinity of adatoms is favourable (as compared to the pristine carbon surface), indicating that the presence of Cl, F or oxygen close or bound to the carbon surface could be beneficial for the initial sodiation and storage, but could also lead to the irreversible entrapment of Na ions and overall capacity loss. Upon Na adsorption, the chlorine desorbs (C-Cl distance evolves from 2.40 Å to 3.24 Å) from the carbon surface, leading to the formation of a Na-Cl dimer; similar dimer formation is observed for Na-F (Figures 4c.ii and 4d.ii), although showing a lower tendency to interact with the carbon surface than F ($E_{ads,F}$=-3.54 eV *vs.* $E_{ads,NaF}$=-2.08 eV). The presence of Na-F and Na-Cl (for the system using the NaClO₄ salt) bond environments in the XPS analysis (Figure 3 g-j) can therefore be unequivocally attributed to the decomposition of the salt in each system.

While the adsorption of F on the carbon surface is more favourable than Cl, the dissociation barrier for ClO₄⁻ is lower than that for PF₆⁻ (0.88 eV *vs.* 1.23 eV, respectively). These results imply that with faster ClO₄⁻ breakdown and subsequent reaction with Na ions, greater irreversible consumption of Na occurs but not localised at the basal plane, consistent with the lower tendency of Cl to remain adsorbed on the carbon ($E_{ads,Cl}$=-2.51 eV *vs.* $E_{ads,F}$=-3.54 eV,). Consequently, the carbon surface remains active for continuous decomposition of ClO₄⁻ anions, resulting in a less stable and non-compact SEI layer; thus, the greater capacity fade observed for EC:DMC/NaClO₄ during cycling may arise from the continuous breakdown of ClO₄⁻ as compared to PF₆⁻ and the growing resistivity arising from the thick SEI, as demonstrated in the EIS before and after cycling (Figure 3 d-f). Conversely, slower consumption of Na ions arising from reaction with PF₆⁻ decomposition fragments but occurring directly at the carbon surface, results in the formation of a thinner, more stable and protective SEI layer and therefore slower capacity loss over subsequent cycles.

Experimentally, these observations are confirmed by the evolution of the NaF band in the XPS which implies that NaF appears to be mainly present in the inner layer of the SEI, as suggested by the increase in percentage with etching time for the systems cycled with NaPF₆.[19] For the NaClO₄ system instead, the NaCl band increases to a lesser extent than the analogous NaF for the NaPF₆ systems, suggesting a more even distribution within the SEI. The presence of NaF has been attributed to a more conductive and protective SEI, and consequently improved cycling stability.[47][48] Conversely, the appearance of NaCl has been linked to a non-compact, insulative and unstable SEI layer that will degrade over time and expose fresh portions of electrode to the electrolyte, promoting further decomposition compounds on the newly developed interfaces.[42][49][50][20] The results from XPS are therefore consistent with the significant deterioration in capacity observed in the NaClO₄ system.

The lower energy barrier to ClO₄⁻ breakdown also leads to oxidative decomposition at the highly reductive surface of the metallic sodium in half cell configuration. XPS analysis of the

sodium-metal counter electrode confirmed the presence of a large amount of NaCl deposits (Figure S14). Since the reversibility of metallic sodium is largely dependent on the composition of the SEI, [47,48,51] the premature failure of this cell may also be ascribed to the rapid and continuous decomposition of the electrolyte at the sodium surface. Qualitative aging experiments (Figure S15) showed that, even without any external voltage, sodium promotes the decomposition of the EC:DMC/NaClO$_4$ electrolyte. Indeed, when our carbon anode is assembled against a Na$_3$V$_2$(PO$_4$)$_2$F$_3$ cathode (NVPF) rather than a sodium metal electrode, the capacity after 200 cycles fades to a minor extent than in the half cell configuration (Figure S16).

Linking the SEI to the intrinsic properties of the salt/solvent system

To rationalise the SEI composition for the different solvent/salt combinations at the atomic scale, *ab initio* molecular dynamics (AIMD) were performed to disseminate the effect of the electrolyte composition on the sodium diffusion and mobility, separating these effects from those arising from the SEI formation and the anode material itself. In diglyme, sodium can coordinate to one, two or three oxygens per diglyme molecule with an average Na-O coordination number of 5.36 at 300 K (Figures S17 and S18 in ESI). This leads to Na being coordinated with two to four diglyme molecules, and the typical solvation shell consisting of two diglyme molecules, in good agreement with previous results.[52] Due to the relatively low polarity and high flexibility of diglyme,[53,54] only one compact coordination shell is observed (derived from AIMD pair distribution functions, see Figures S17, S18 and S19 in ESI). The PF$_6^-$ anion remains intact during the whole simulation, only interacting with the terminal aliphatic hydrogens of diglyme. Well in agreement with previous observations,[49] this lack of interaction beyond the solvation shell for Na$^+$ confirms that diglyme can effectively keep the anion away from the cation, remaining 10.28 ±1Å apart on average (a plot showing the cation-anion distance is provided in the ESI in Fig S20). For the EC:DMC based electrolytes, the cation-anion distance is longer than the corresponding distance in the diglyme electrolyte (11.92±0.7 Å for Na-PF$_6$, and 12.21±0.8 Å for NaClO$_4$). For the EC:DMC systems, both carbonyl and ester oxygens enable a strong interaction with Na$^+$. Additionally, due to the high polarity and relatively high rigidity of the solvent molecules, two bulky and non-compact solvation shells were identified for both NaPF$_6$ and NaClO$_4$ salts (see tables S3 and S4 in the SEI and complementary explanation). The average coordination numbers for the first Na-O coordination shell at 300 K are 5.12 and 5.15 for NaPF$_6$ and NaClO$_4$, respectively, while in the second coordination shell, the average coordination increases to 12 for both salts.

The differences in solvation for the anions (PF$_6^-$ and ClO$_4^-$) and Na$^+$ in the two solvent systems are responsible of the differences in ionic transport, diffusion coefficient (D$_{Na}$ and D$_{Anion}$), and sodium transport number (t) derived from our simulations (Table 1).

Table 1. *Calculated diffusion coefficients (D), activation energies (E$_a$), and transport number (t) for the different solvent electrolyte systems from AIMD simulations at 300K.*

Solvent	Salt	D$_{Na+}$ (×10^{5}cm^{2}s^{-1})	D$_{Anion-}$ (×10^5 cm^{2}s^{-1})	t
Diglyme	NaPF$_6$	1.61	3.24	0.33
EC:DMC		1.16	1.84	0.39
	NaClO$_4$	1.31	1.65	0.44

NaPF$_6$ vs. NaClO$_4$ in EC:DMC. The calculated D$_{Na}$ is similar for both the NaPF$_6$ and NaClO$_4$ salts in EC:DMC (Table 1). Thus, the diffusion of Na$^+$ through the electrolyte bulk appears to

have limited direct impact on the electrochemical performance observed for these systems, indicating that the difference in both the short- and long-term capacity observed between the $NaPF_6$ and $NaClO_4$ cells arises due to processes occurring at the electrode surfaces.

The transport number (t) is a measurement of the mobility of the cation relative to the counterion,[18,55] and indicates that the movement of Na^+ and ClO_4^- ions are better correlated than Na^+ with PF_6^- ions in EC:DMC. ClO_4^- has a high donor number compared to PF_6^- (8.44 vs. 2.5 respectively) closer to that of EC:DMC (16-17). ClO_4^- can thus more effectively compete with the EC:DMC molecules to solvate Na^+ resulting in minimal ion separation. These results suggest that as Na^+ approaches the carbon electrode, far more ClO_4^- than PF_6^- anions are brought within close proximity of both the Na^+ and the carbon surface, promoting greater decomposition of the anion, and corroborating the experimental results above.

$NaPF_6$ in EC:DMC vs. $NaPF_6$ in diglyme. Swapping EC:DMC for diglyme whilst keeping the $NaPF_6$ salt showed an increase in the D_{Na},(Table 1) indicating that Na diffusion in the diglyme system is more rapid. Interestingly, the diffusion of PF_6^- is also notably higher than for the other systems,[55] but the low value of (*t*) implies the lowest cation-anion mobility correlation in diglyme, suggesting that even if both PF_6^- and Na^+ are more mobile in diglyme, Na^+ is more protected and separated from the PF_6^- anion. Therefore, the degree of interaction between PF_6^- anions and the HC surface is even lower in diglyme compared with EC:DMC, resulting in far less decomposition and thus much less consumption of Na within the thinner SEI layer. Furthermore, PF_6^- has a higher reduction potential than diglyme[21][56] which leads to preferential decomposition of the anion before the solvent, to stabilise the surface to further decomposition. Meanwhile, comparing the reduction potentials of diglyme with EC:DMC, EC:DMC is much more easily reduced and will result in a subsequent greater organic contribution to the SEI layer,[57] as has been demonstrated by XPS.

In summary, the first cycle and long-term electrochemical behaviours of the different electrolyte systems are dependent on the interactions of the Na ions with the solvent molecules and anions (Figure 5), and the subsequent decomposition behaviour at the electrode surface.
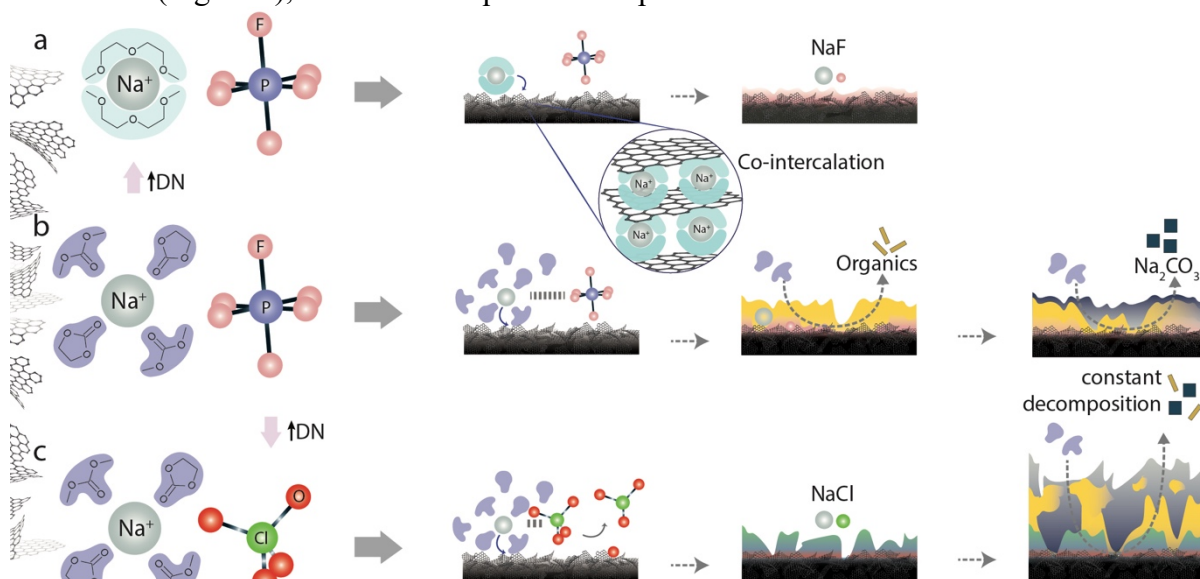

Figure 5. *Schematic representation of the SEI formation in: **(a)** 1M $NaPF_6$/Diglyme,where a thin and homogenous layer of Na-F formed from the decomposition of $NaPF_6$ serves as a Na-conductive and protective layer for the further stable cycling of the HC electrode; **(b)** 1M $NaPF_6$/EC:DMC, where a Na-F protective layer forms, however, due to worse solvation of Na^+, organic compounds derived from the electrochemical decomposition of the solvent increase the intefacial resistance and in turn lower the long-term stability of the anode; **(c)** 1M*

NaClO$_4$/EC:DMC, where the decomposition of ClO$_4^-$ enables oxygen functionalisation on the carbon that can irreversibly trap Na$^+$, and formation of a non protective NaCl layer that contributes to the premature failure of the cell.

We suggest that NaClO$_4$ in EC:DMC (Figure 5c) achieves a higher first cycle capacity than NaPF$_6$ because the incorporation of ClO$_4^-$ decomposition products (oxygen, red spheres in figure 5c) into the carbon basal plane can provide additional Na storage capability. However, the capacity fades quickly since unstable adsorption of other ClO$_4^-$ fragments leaves the carbon surface available for constant decomposition and subsequent Na consumption. The SEI layer is evenly composed of NaCl and organics such as Na$_2$CO$_3$ and C=O species, and is thicker than the SEI produced in the NaPF$_6$ systems. NaCl leads to a non-conductive SEI, and it is this increased resistance, as well as the continuous Na ion consumption, that results in deteriorating performance in subsequent cycles. In the NaPF$_6$ systems (Figure 5a and b), strong initial adsorption of F fragments results in subsequent stable adsorption of Na ions, leading to the controlled formation of a compact protective SEI. As NaF is more Na-conductive than NaCl, and deposits stably onto the carbon surface, subsequent decomposition of the anion is mostly suppressed, resulting in greater long-term cycling stability. However, changing the solvent has a great effect on both initial and long-term capacity. With diglyme (Figure 5a), the more compact solvation shell could allow a certain degree of co-intercalation, thus limiting the overall initial capacity. The significantly superior capacity retention arises from the very limited degree of solvent degradation reducing the total amount of Na irreversibly consumed, and also the formation of a less resistive SEI layer mostly formed of NaF. We suggest that it is the structure of this largely inorganic internal SEI layer that promotes excellent long-term stability in NaPF$_6$/diglyme. As observed by XPS (Figure 3g-j), the structure of the SEI layer formed in EC:DMC (Figure 5b) consists of an inner NaF-rich layer too; however, in this case, the appearance of a largely organic outermost layer composed of the electrochemical reduction products of the solvent is evident and contributes to increased resistivity. This layer might arise as a consequence of to the larger de-solvation energy barrier that Na$^+$ needs to overcome in the carbonate-based solvent[58][59][60] and the greater possibility of PF$_6^-$ to penetrate into the carbonate solvation shell in comparison to the Na-diglyme system.

Conclusion.

In this study, we synthesised a range of hard carbons with bimodal native and templated porosity for use as NIB electrodes. The material with the greatest closed porosity exhibited the highest capacity across a range of current densities, due to the optimised structure of enlarged interlayer distances and mesopores preserving connectivity between the native micropores. The ST1500 material was further investigated with alternative electrolyte systems and the choice solvent and salt were shown to have a significant effect on long-term cycling performance. Through a combination of XPS and theoretical modelling, we have demonstrated that the presence of F-containing species in the electrolyte is important for the formation of a compact, ion-conducting protective layer, whilst the solvent choice can further improve or impair electrochemical performance, depending on the interaction with both cations and anions in solution. These findings highlight the importance not only of considering active material suitability but also selecting appropriate electrolyte systems in order to obtain optimised performance for future sodium ion batteries.

EXPERIMENTAL METHODS

Materials synthesis. All chemicals were purchased from Sigma-Aldrich and used as received if not specified otherwise.

Soft templated carbons: For the synthesis of the soft templated carbons, a precursor solution was carbonised under autogenic pressure at 200 °C. In a typical experiment, 0.82 g phloroglucinol (1,3,5-benzentriol, $C_6H_6O_3$) and 0.61 g of glyoxylic acid monohydrate were mixed with 1.61 g Pluronic F127 triblock copolymer and dissolved in 40 ml of absolute ethanol. [22] The solution was transferred into a 100 ml Teflon autoclave liner, sealed (Parr Instruments stainless steel autoclave) and placed in an oven at 80 °C for 4 h to trigger the phloroglucinol/glyoxylic acid crosslinking reaction. Subsequently, the mixture was solvothermally carbonised at 200 °C for 12 h. After cooling, the suspension was filtered, and the solid fraction was dried under vacuum at 40 °C for 12h. The dry material was then annealed up to 1000, 1300, and 1500 ºC at a rate of 5 ºC min^{-1} for 2h.

Cathode for full cell testing: The NVPF@C cathode material was synthesized following a hydrothermal method.[61] A typical synthesis is as follows: 0.98g V_2O_5 and 0.337g oxalic acid were added into 15 mL deionized water under continuous magnetic stirring at 70 °C for 20 min. Subsequently $NH_4H_2PO_4$ (0.252 g), NaF (0.130 g) and 0.03 g of carbon black (Super P conductive, 99+%, Alfa Aesar) were added into the blue solution under stirring. The obtained mixture was transferred to 50 mL Teflon liners, which were then placed inside stainless steel autoclaves and kept at 180 °C for 12 h. After this time, the obtained gel was freeze-dried and subsequently annealed under argon at 475 °C for 9 h using a heating rate of 5°C min^{-1}. For sake of comparison, an NVPF sample without Super P carbon was also prepared using the same methodology and annealing procedure.

Materials characterisation

Morphological investigations were carried out by using a FEI Inspect F SEM operated at 10 kV. Transmission electron microscopy (TEM) was carried out using a JEOL 2100Plus TEM at 200 kV operating voltage. N_2 and CO_2 adsorption isotherms were measured by using a Micromeritics ASAP 2020 instrument. Prior to the analysis the materials were degassed overnight under vacuum at 200 °C. The BET surface area (S_{BET}) was calculated in the relative pressure range of 0.05–0.3 for N_2 adsorption and the micropore surface area (S_{CO2}) was determined using the Dubinin–Radushkevich (DR) method. The pore size distribution was assessed by density functional theory (DFT) for slit pores. Raman spectra were recorded in a Raman-Senterra II spectrometer equipped with a 100X objective and a 532 nm laser as excitation source.

Small/wide angle X-ray scattering (SAXS/WAXS) was measured on a Xenocs nano-InXider with a Cu k$_\alpha$ source and a two-detector setup for combined SAXS/WAXS measurements. Powder samples were packed in 2 mm Kapton capillaries and measured for 10 min. The empty capillary was measured separately and used for background subtraction. Neutron total scattering was carried out at the NIMROD [62]instrument at ISIS (Harwell, UK). Each sample was measured for 2 hours and data corrections and reduction were performed using Gudrun.[63]

Electrochemical characterisation

Electrodes were made using an 85:5:10 weight ratio of active material, carbon black (Super P conductive, 99+%, Alfa Aesar), and carboxymethyl cellulose binder (CMC) (Mw~250,000, Sigma Aldrich), respectively. A 250 μm layer of the slurry was then coated onto a carbon coated aluminium foil (18 μm conductive coating, MTI corporation) through blade casting (doctor blade coater). Once dried at room temperature for 24h, 13mm discs were cut and dried at 100˚C for 2 h under vacuum. The electrolyte preparation and coin cell assembly were conducted in an argon-filled glovebox (MBraun GmbH Labstar glovebox workstation) with H_2O < 0.5 ppm and O_2 < 0.5 ppm levels. CR2032 coin cells were assembled using sodium

metal counter electrode discs (less than 0.5mm thick, rolled and cut from a sodium ingot, 99.8% metals basis, Alfa Aesar), the coated hard carbon as working electrodes and a glass fibre separator (Whatman GF/B glass microfibre, 18 mm diameter) saturated with electrolyte (150 µL). For the evaluation of full cells, the NVPF@C material was coated and cut in the same manner than the hard carbons, tested first against sodium metal and subsequently assembled with our hard carbon materials as anodes. All electrolytes were prepared with a 1M salt concentration. Either sodium hexafluorophosphate (NaPF$_6$ Alfa Aesar, 99+%) or sodium perchlorate (NaClO$_4$, 99.9+%, Sigma Aldrich) were dissolved in the pre-dried solvents (80 °C overnight and then placed in a bottle containing 4 Å porous molecular sieve). For the 1:1 volume mixture of ethylene carbonate (EC, anhydrous 99%, Sigma Aldrich) and dimethyl carbonate (DMC, 99.9+%, Sigma Aldrich), EC was first heated up to 45 °C inside the glovebox antechamber and them stirred with an equal volume of DMC until fully homogeneous. When diethylene glycol dimethyl ether was used (diglyme, anhydrous, 99.5%, Sigma Aldrich), the salt was directly added and stirred until complete dissolution. Galvanostatic cycling tests were performed on a Basytec system in the potential range of 0.001-2.5 V *vs.* Na+/Na and using sodiation/desodiation current rates between 30 and 600 mA g^{-1}, corresponding to cycle rates between 0.1 and 2C based on a theoretical capacity of 300 mAh g^{-1}. Cyclic voltammetry (CV) and electrochemical impedance spectroscopy (EIS) were performed on a Biologic VSP-300 potentiostat. CVs were recorded at a scan rate of 0.1 mV s^{-1} for 5 cycles and EIS data was collected between 200 kHz and 10 mHz with a signal amplitude of 10 mV.

References
1. Armand, M., and Tarascon, J.M. (2008) Building better batteries. *Nature*, **451** (7179), 652–657.
2. Grosjean, C., Miranda, P., Perrin, M., Sustainable, P.P.-R. and, and 2012, undefined Assessment of world lithium resources and consequences of their geographic distribution on the expected development of the electric vehicle industry. *Elsevier*.
3. Kubota, K., Society, S.K.-J. of T.E., and 2015, undefined (2015) Review-Practical Issues and Future Perspective for Na-Ion Batteries. *iopscience.iop.org*, **162** (14), A2538–A2550.
4. Stevens, D.A., and Dahn, J.R. (2000) High Capacity Anode Materials for Rechargeable Sodium-Ion Batteries. *J. Electrochem. Soc.*, **147** (4), 1271.
5. Titirici, M.M., Alptekin, H., Au, H., Jensen, A.C.S., Olsson, E., Goktas, M., Headen, T.F., Adelhelm, P., Cai, Q., and Drew, A.J. (2020) Sodium storage mechanism investigations through structural changes in hard carbons. *ACS Appl. Energy Mater.*, **3** (10), 9918–9927.
6. Jensen, A.C.S., Olsson, E., Au, H., Alptekin, H., Yang, Z., Cottrell, S., Yokoyama, K., Cai, Q., Titirici, M.M., and Drew, A.J. (2020) Local mobility in electrochemically inactive sodium in hard carbon anodes after the first cycle. *J. Mater. Chem. A*, **8** (2), 743–749.
7. Li, Y., Lu, Y., Meng, Q., Jensen, A.C.S., Zhang, Q., Zhang, Q., Tong, Y., Qi, Y., Gu, L., Titirici, M., and Hu, Y. (2019) Regulating Pore Structure of Hierarchical Porous Waste Cork-Derived Hard Carbon Anode for Enhanced Na Storage Performance. *Adv. Energy Mater.*, **9** (48), 1902852.
8. Meng, Q., Lu, Y., Ding, F., Zhang, Q., Chen, L., and Hu, Y.S. (2019) Tuning the Closed Pore Structure of Hard Carbons with the Highest Na Storage Capacity. *ACS Energy Lett.*, **4** (11), 2608–2612.
9. Yamamoto, H., Muratsubaki, S., Kubota, K., Fukunishi, M., Watanabe, H., Kim, J., and Komaba, S. (2018) Synthesizing higher-capacity hard-carbons from cellulose for Na- and K-ion batteries. *J. Mater. Chem. A*, **6** (35), 16844–16848.

10. Au, H., Alptekin, H., Jensen, A.C.S., Olsson, E., O'Keefe, C.A., Smith, T., Crespo-Ribadeneyra, M., Headen, T.F., Grey, C.P., Cai, Q., Drew, A.J., and Titirici, M.-M. (2020) A revised mechanistic model for sodium insertion in hard carbons. *Energy Environ. Sci.*

11. Kamiyama, A., Kubota, K., Igarashi, D., Youn, Y., Tateyama, Y., Ando, H., Gotoh, K., and Komaba, S. (2021) MgO-Template Synthesis of Extremely High Capacity Hard Carbon for Na-Ion Battery. *Angew. Chemie - Int. Ed.*, **60** (10), 5114–5120.

12. Carboni, M., Manzi, J., Armstrong, A.R., Billaud, J., Brutti, S., and Younesi, R. (2019) Analysis of the Solid Electrolyte Interphase on Hard Carbon Electrodes in Sodium-Ion Batteries. *ChemElectroChem*, **6** (6), 1745–1753.

13. Komaba, S., Ishikawa, T., Yabuuchi, N., Murata, W., Ito, A., and Ohsawa, Y. (2011) Fluorinated ethylene carbonate as electrolyte additive for rechargeable Na batteries. *ACS Appl. Mater. Interfaces*, **3** (11), 4165–4168.

14. Li, K., Zhang, J., Lin, D., Wang, D.W., Li, B., Lv, W., Sun, S., He, Y.B., Kang, F., Yang, Q.H., Zhou, L., and Zhang, T.Y. (2019) Evolution of the electrochemical interface in sodium ion batteries with ether electrolytes. *Nat. Commun.*, **10** (1), 1–10.

15. Goktas, M., Bolli, C., Buchheim, J., Berg, E.J., Novák, P.N., Bonilla, F., Teófilo, ⊥, Rojo, T., Komaba, S., Kubota, K., and Adelhelm, P. (2019) Stable and Unstable Diglyme-Based Electrolytes for Batteries with Sodium or Graphite as Electrode.

16. Zhang, J., Wang, D.W., Lv, W., Zhang, S., Liang, Q., Zheng, D., Kang, F., and Yang, Q.H. (2017) Achieving superb sodium storage performance on carbon anodes through an ether-derived solid electrolyte interphase. *Energy Environ. Sci.*, **10** (1), 370–376.

17. Pan, Y., Zhang, Y., Parimalam, B.S., Nguyen, C.C., Wang, G., and Lucht, B.L. (2017) Investigation of the solid electrolyte interphase on hard carbon electrode for sodium ion batteries. *J. Electroanal. Chem.*, **799**, 181–186.

18. Kamath, G., Cutler, R.W., Deshmukh, S.A., Shakourian-Fard, M., Parrish, R., Huether, J., Butt, D.P., Xiong, H., and Sankaranarayanan, S.K.R.S. (2014) In silico based rank-order determination and experiments on nonaqueous electrolytes for sodium ion battery applications. *J. Phys. Chem. C*, **118** (25), 13406–13416.

19. Fondard, J., Irisarri, E., Courrèges, C., Palacin, M.R., Ponrouch, A., and Dedryvère, R. (2020) SEI Composition on Hard Carbon in Na-Ion Batteries After Long Cycling: Influence of Salts (NaPF 6 , NaTFSI) and Additives (FEC, DMCF) . *J. Electrochem. Soc.*, **167** (7), 070526.

20. Ponrouch, A., Marchante, E., Courty, M., Tarascon, J.M., and Palacín, M.R. (2012) In search of an optimized electrolyte for Na-ion batteries. *Energy Environ. Sci.*, **5** (9), 8572–8583.

21. Westman, K., Dugas, R., Jankowski, P., Wieczorek, W., Gachot, G., Morcrette, M., Irisarri, E., Ponrouch, A., Palacín, M.R., Tarascon, J.M., and Johansson, P. (2018) Diglyme Based Electrolytes for Sodium-Ion Batteries. *ACS Appl. Energy Mater.*, **1** (6), 2671–2680.

22. Matei Ghimbeu, C., Vidal, L., Delmotte, L., Le Meins, J.M., and Vix-Guterl, C. (2014) Catalyst-free soft-template synthesis of ordered mesoporous carbon tailored using phloroglucinol/glyoxylic acid environmentally friendly precursors. *Green Chem.*, **16** (6), 3079–3088.

23. Beda, A., Taberna, P.-L., Simon, P., and Matei Ghimbeu, C. (2018) Hard carbons derived from green phenolic resins for Na-ion batteries. *Carbon N. Y.*, **139**, 248–257.

24. Meng, Q., Lu, Y., Ding, F., Zhang, Q., Chen, L., and Hu, Y.S. (2019) Tuning the Closed Pore Structure of Hard Carbons with the Highest Na Storage Capacity. *ACS Energy Lett.*, **4** (11), 2608–2612.

25. Xie, F., Xu, Z., Jensen, A.C.S., Au, H., Lu, Y., Araullo-Peters, V., Drew, A.J., Hu, Y.-

S., and Titirici, M.-M. (2019) Hard–Soft Carbon Composite Anodes with Synergistic Sodium Storage Performance. *Adv. Funct. Mater.*, **29** (24), 1901072.

26. Stevens, D.A., and Dahn, J.R. (2000) An In Situ Small-Angle X-Ray Scattering Study of Sodium Insertion into a Nanoporous Carbon Anode Material within an Operating Electrochemical Cell. *J. Electrochem. Soc.*, **147** (12), 4428.

27. Hammouda, B. (2010) A new Guinier-Porod model. *J. Appl. Crystallogr.*, **43** (4), 716–719.

28. Kamiyama, A., Kubota, K., Nakano, T., Fujimura, S., Shiraishi, S., Tsukada, H., and Komaba, S. (2020) High-Capacity Hard Carbon Synthesized from Macroporous Phenolic Resin for Sodium-Ion and Potassium-Ion Battery. *ACS Appl. Energy Mater.*, **3** (1), 135–140.

29. Ravikovitch, P.I., Vishnyakov, A., Russo, R., and Neimark, A. V. (2000) Unified approach to pore size characterization of microporous carbonaceous materials from N2, Ar, and CO2 adsorption isotherms. *Langmuir*, **16** (5), 2311–2320.

30. Kubota, K., Shimadzu, S., Yabuuchi, N., Tominaka, S., Shiraishi, S., Abreu-Sepulveda, M., Manivannan, A., Gotoh, K., Fukunishi, M., Dahbi, M., and Komaba, S. (2020) Structural Analysis of Sucrose-Derived Hard Carbon and Correlation with the Electrochemical Properties for Lithium, Sodium, and Potassium Insertion. *Chem. Mater.*, **32** (7), 2961–2977.

31. Dou, X., Hasa, I., Saurel, D., Vaalma, C., Wu, L., Buchholz, D., Bresser, D., Komaba, S., and Passerini, S. (2019) Hard carbons for sodium-ion batteries: Structure, analysis, sustainability, and electrochemistry. *Mater. Today*, **23**, 87–104.

32. Herou, S., Ribadeneyra, M.C., Madhu, R., Araullo-Peters, V., Jensen, A., Schlee, P., and Titirici, M. (2019) Ordered mesoporous carbons from lignin: a new class of biobased electrodes for supercapacitors. *Green Chem.*, **21** (3), 550–559.

33. Ferrari, A., and Robertson, J. (2000) Interpretation of Raman spectra of disordered and amorphous carbon. *Phys. Rev. B - Condens. Matter Mater. Phys.*, **61** (20), 14095–14107.

34. Komaba, S., Murata, W., Ishikawa, T., Yabuuchi, N., Ozeki, T., Nakayama, T., Ogata, A., Gotoh, K., and Fujiwara, K. (2011) Electrochemical Na insertion and solid electrolyte interphase for hard-carbon electrodes and application to Na-ion batteries. *Adv. Funct. Mater.*, **21** (20), 3859–3867.

35. Che, H., Chen, S., Xie, Y., Wang, H., Amine, K., Liao, X.Z., and Ma, Z.F. (2017) Electrolyte design strategies and research progress for room-temperature sodium-ion batteries. *Energy Environ. Sci.*, **10** (5), 1075–1101.

36. Schmeisser, M., Illner, P., Puchta, R., Zahl, A., and van Eldik, R. (2012) Gutmann Donor and Acceptor Numbers for Ionic Liquids. *Chem. - A Eur. J.*, **18** (35), 10969–10982.

37. Tobishima, S., Morimoto, H., Aoki, M., Saito, Y., Inose, T., Fukumoto, T., and Kuryu, T. (2004) Glyme-based nonaqueous electrolytes for rechargeable lithium cells. *Electrochim. Acta*, **49** (6), 979–987.

38. Jache, B., Binder, J.O., Abe, T., and Adelhelm, P. (2016) A comparative study on the impact of different glymes and their derivatives as electrolyte solvents for graphite co-intercalation electrodes in lithium-ion and sodium-ion batteries. *Phys. Chem. Chem. Phys.*, **18** (21), 14299–14316.

39. Inagaki, M., and Tanaike, O. (1995) Host effect on the formation of sodium-tetrahydrofuran-graphite intercalation compounds. *Synth. Met.*, **73** (1), 77–81.

40. Zhang, H., and Lerner, M.M. (2016) Preparation of Graphite Intercalation Compounds Containing Crown Ethers. *Inorg. Chem.*, **55** (17), 8281–8284.

41. Au, H., Rubio, N., Buckley, D.J., Mattevi, C., and Shaffer, M.S.P. (2020) Thermal

Decomposition of Ternary Sodium Graphite Intercalation Compounds. *Chem. - A Eur. J.*, **26** (29), 6545–6553.

42. Lutz, L., Alves Dalla Corte, D., Tang, M., Salager, E., Deschamps, M., Grimaud, A., Johnson, L., Bruce, P.G., and Tarascon, J.M. (2017) Role of Electrolyte Anions in the Na-O2Battery: Implications for NaO2Solvation and the Stability of the Sodium Solid Electrolyte Interphase in Glyme Ethers. *Chem. Mater.*, **29** (14), 6066–6075.

43. López, G.P., Castner, D.G., and Ratner, B.D. (1991) XPS O 1s binding energies for polymers containing hydroxyl, ether, ketone and ester groups. *Surf. Interface Anal.*, **17** (5), 267–272.

44. Olsson, E., Chai, G., Dove, M., and Cai, Q. (2019) Adsorption and migration of alkali metals (Li, Na, and K) on pristine and defective graphene surfaces. *Nanoscale*, **11** (12), 5274–5284.

45. Olsson, E., Cottom, J., Au, H., Titirici, M.M., and Cai, Q. (2021) Investigating the effect of edge and basal plane surface functionalisation of carbonaceous anodes for alkali metal (Li/Na/K) ion batteries. *Carbon N. Y.*, **177**, 226–243.

46. Nakada, K., and Ishii, A. (2011) Migration of adatom adsorption on graphene using DFT calculation. *Solid State Commun.*, **151** (1), 13–16.

47. Fan, X., Ji, X., Han, F., Yue, J., Chen, J., Chen, L., Deng, T., Jiang, J., and Wang, C. (2018) Fluorinated solid electrolyte interphase enables highly reversible solid-state Li metal battery. *Sci. Adv.*, **4** (12), 9245.

48. He, M., Guo, R., Hobold, G.M., Gao, H., and Gallant, B.M. (2020) The intrinsic behavior of lithium fluoride in solid electrolyte interphases on lithium. *Proc. Natl. Acad. Sci.*, **117** (1), 73–79.

49. Zhou, L., Cao, Z., Wahyudi, W., Zhang, J., Hwang, J.-Y., Cheng, Y., Wang, L., Cavallo, L., Anthopoulos, T., Sun, Y.-K., Alshareef, H.N., and Ming, J. (2020) Electrolyte Engineering Enables High Stability and Capacity Alloying Anodes for Sodium and Potassium Ion Batteries. *ACS Energy Lett.*, **5** (3), 766–776.

50. Gangaja, B., Nair, S., and Santhanagopalan, D. (2019) Solvent-controlled solid-electrolyte interphase layer composition of a high performance Li4Ti5O12 anode for Na-ion battery applications. *Sustain. Energy Fuels*, **3** (9), 2490–2498.

51. Choudhury, S., Wei, S., Ozhabes, Y., Gunceler, D., Zachman, M.J., Tu, Z., Shin, J.H., Nath, P., Agrawal, A., Kourkoutis, L.F., Arias, T.A., and Archer, L.A. Designing solid-liquid interphases for sodium batteries.

52. Jensen, A.C.S., Au, H., Gärtner, S., Titirici, M., and Drew, A.J. (2020) Solvation of NaPF 6 in Diglyme Solution for Battery Electrolytes . *Batter. Supercaps*, **3** (12), 1306–1310.

53. Khan, M.S., Karatrantos, A. V., Ohba, T., and Cai, Q. (2019) The effect of different organic solvents and anion salts on sodium ion storage in cylindrical carbon nanopores. *Phys. Chem. Chem. Phys.*, **21** (41), 22722–22731.

54. Karatrantos, A., Khan, S., Ohba, T., and Cai, Q. (2018) The effect of different organic solvents on sodium ion storage in carbon nanopores. *Phys. Chem. Chem. Phys.*, **20** (9), 6307–6315.

55. Morales, D., Ruther, R.E., Nanda, J., and Greenbaum, S. (2019) Ion transport and association study of glyme-based electrolytes with lithium and sodium salts. *Electrochim. Acta*, **304**, 239–245.

56. Jó, E., and Johansson, P. (2015) Electrochemical oxidation stability of anions for modern battery electrolytes: a CBS and DFT study †. *Phys. Chem. Chem. Phys*, **17**, 3697.

57. Eshetu, G.G., Elia, G.A., Armand, M., Forsyth, M., Komaba, S., Rojo, T., and Passerini, S. (2020) Electrolytes and Interphases in Sodium-Based Rechargeable

Batteries: Recent Advances and Perspectives. *Adv. Energy Mater.*, **10** (20).

58. Liu, Q., Wu, F., Mu, D., and Wu, B. (2020) A theoretical study on Na+ solvation in carbonate ester and ether solvents for sodium-ion batteries. *Phys. Chem. Chem. Phys.*, **22** (4), 2164–2175.

59. Yoshida, K., Nakamura, M., Kazue, Y., Tachikawa, N., Tsuzuki, S., Seki, S., Dokko, K., and Watanabe, M. (2011) Oxidative-stability enhancement and charge transport mechanism in glyme-lithium salt equimolar complexes. *J. Am. Chem. Soc.*, **133** (33), 13121–13129.

60. Xu, K., Von Cresce, A., and Lee, U. (2010) Differentiating Contributions to "Ion Transfer" Barrier from Interphasial Resistance and Li þ Desolvation at Electrolyte/Graphite Interface. *Langmuir*, **26** (13), 11538–11543.

61. Cai, Y., Cao, X., Luo, Z., Fang, G., Liu, F., Zhou, J., Pan, A., and Liang, S. (2018) Caging Na3V2(PO4)2F3 Microcubes in Cross-Linked Graphene Enabling Ultrafast Sodium Storage and Long-Term Cycling. *Adv. Sci.*, **5** (9).

62. Bowron, D.T., Soper, A.K., Jones, K., Ansell, S., Birch, S., Norris, J., Perrott, L., Riedel, D., Rhodes, N.J., Wakefield, S.R., Botti, A., Ricci, M.-A., Grazzi, F., and Zoppi, M. (2010) NIMROD: The Near and InterMediate Range Order Diffractometer of the ISIS second target station. *Rev. Sci. Instrum.*, **81** (3), 033905.

63. Soper, A.K. (2011) Rutherford Appleton Laboratory Technical Report RAL-TR-2011-013. (July).